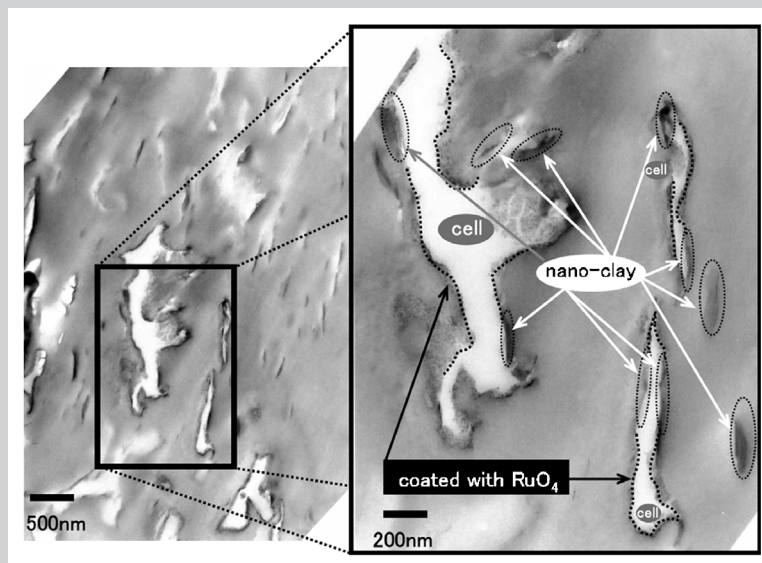


Summary: Via a batch process in an autoclave, foam processing of intercalated PC/clay nanocomposites, having different amounts of clay, has been conducted using supercritical CO₂ as a foaming agent. The cellular structures obtained from various foaming temperature-CO₂ pressure ranges were investigated by SEM. The incorporation with nanoclay-induced heterogeneous nucleation occurs because of a lower

activation energy barrier compared with homogeneous nucleation as revealed by the characterization of the interfacial tension between bubble and matrix. The controlled structure of the PCCN foams changed from microcellular ($d \cong 20 \mu\text{m}$ and $N_c \cong 1.0 \times 10^9 \text{ cells} \cdot \text{cm}^{-3}$) to nanocellular ($d \cong 600 \text{ nm}$ and $N_c \cong 3.0 \times 10^{13} \text{ cells} \cdot \text{cm}^{-3}$). The mechanical properties of PCCN foams under compression test were discussed.



TEM micrograph for the structure of the cell wall foamed at 160 °C.

Foam Processing and Cellular Structure of Polycarbonate-Based Nanocomposites

Yasuhito Ito, Masatoshi Yamashita, Masami Okamoto*

Advanced Polymeric Nanostructured Materials Engineering, Graduate School of Engineering,
Toyota Technological Institute, Hisakata 2-12-1, Tempaku, Nagoya 468-8511, Japan
E-mail: okamoto@toyota-ti.ac.jp

Received: February 10, 2006; Revised: April 5, 2006; Accepted: April 5, 2006; DOI: 10.1002/mame.200600075

Keywords: heterogeneous nucleation; nanocellular; nanocomposite foams; polycarbonate; supercritical carbon dioxide

Introduction

Development of nanocomposite foams is one of the latest evolutionary technologies of the polymeric foam through a pioneering effort by Okamoto and his colleagues.^[1,2] They prepared intercalated polycarbonate (PC)/clay nanocomposite (PCCN) foams in a batch process, by using supercritical CO₂ as a physical foaming agent.^[3] The PCCN

foam exhibited smaller cell size and larger cell density compared with neat PC foam. However there are still some controversial data regarding the nucleating effect of the dispersed clay particles.

To innovate on the materials properties of nanocomposites foams, we have to understand the morphology correlation between the dispersed clay particles with nanometer dimensions in the bulk and formed closed-cell structure after

Table 1. Composition and characteristic parameters of various PCCNs.

	Composition	$10^{-4} M_V^b)$	$T_g^c)$	Modulus ^{d)}
	PC SMA MAE ^{a)}			
	wt.-%	$g \cdot mol^{-1}$	$^{\circ}C$	GPa
PC/SMA	90 10	2.43	146	2.32
PC/SMA/MAE1	96.4 2 1.6 [1.0]	2.11	144	2.63
PC/SMA/MAE2.5	91 5 4 [2.5]	1.93	134	3.10
PC/SMA/MAE5	82 10 8 [5.0]	1.85	107	4.15

^{a)} Value in the parentheses indicates the amount of clay (inorganic part) content after burning.

^{b)} Viscosity-average molecular weight.^[3]

^{c)} The glass transition temperature.^[3]

^{d)} Flexural modulus and strength of the injection-molded specimens (thickness ≈ 3.2 mm) were measured according to ASTM D-790 method (Model 2020, Intesco Co.) with a strain rate of $2 \text{ mm} \cdot \text{min}^{-1}$ at room temperature.^[3]

foaming. To the best of our knowledge, however, this issue is not very well explored in the literature. There has been no research reported so far on systematic studies on the preparation of nanocomposite foams from microcellular to nanocellular. This paper is devoted to the study and evaluation of the performance potential of the PCCNs in foam applications. We investigate the influence of clay loading to the morphology of PCCN foams.

Experimental Part

Materials

PC with viscosity-average molecular weight \bar{M}_V of 2.40×10^4 (Teijin Chemicals Ltd., Japan) was dried under vacuum at $120^{\circ}C$ and kept under a dry nitrogen gas for one week prior to use. In this study, we used a synthetic fluorohectorite (*syn-FH*) as an organically modified clay, which was supplied by CO-OP Chemical Co. Ltd. The organically modified synthetic fluorohectorite was synthesized by replacing Na^+ in *syn-FH* of a cation exchange capacity of 120 milliequiv. per 100 g (original thickness of ≈ 1 nm and average length of 200–300 nm) with

the dimethyl dioctadecylammonium cation (MAE) by ion exchange reaction.

The compatibilizer poly[styrene-*co*-(maleic anhydride)] (SMA) with 15 wt.-% MA content, number-average molecular weight \bar{M}_n of 17.1×10^4 (DYLARK 332-80) was supplied by Nova Chemical Japan Ltd.

Nanocomposites Preparation and Characterization

Nanocomposites were prepared by melt extrusion. MAE (powder form) and SMA as a compatibilizer (pellets form) were first dry-mixed by shaking them in a bag. The mixture was then melt extruded using a twin-screw extruder (PCM-30, Ikegai machinery Co.) operated at $240^{\circ}C$ (screw speed = 100 rpm, feed rate = $120 \text{ g} \cdot \text{min}^{-1}$) to yield SMA/MAE-intercalated nanocomposites strands. The strands were then pelletized, and loaded with PC pellets. The mixture was again extruded by melt mixing operated at $260^{\circ}C$. The abbreviations of various nanocomposites (PCCNs) prepared using three different content of MAE are shown in Table 1. The details of the nanocomposites preparation were described in our previous paper.^[3] The extruded strands were pelletized and dried under vacuum at $120^{\circ}C$ for 24 h to remove water. The

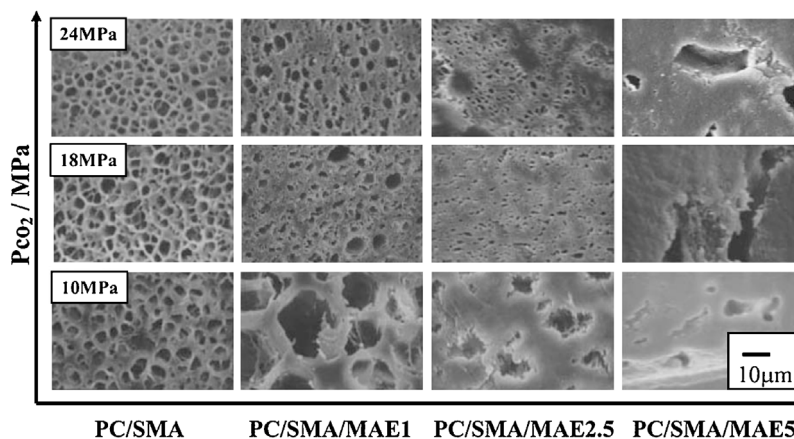


Figure 1. Typical SEM images of the fracture surfaces of the PC/SMA and PCCNs foamed at $140^{\circ}C$ under different isobaric condition (10, 18 and 24 MPa).

nanostructure analyses of wide-angle X-ray diffraction (WAXD) and transmission electron microscopy (TEM) were carried out using the same apparatus as described in the previous articles.^[1–3]

Foam Processing

The foam processing was conducted on PC/SMA and PCCNs in an autoclave (TSC-WC-0096, Taiatsu Techno Co) by using supercritical CO₂.^[2] Before foaming, the test samples were dried under vacuum at 100 °C for 8 h to remove the water. Basically, the physical foam processing (batch process) used in this study consists of three stages: (1) CO₂ saturation of the sample under supercritical CO₂; (2) cell nucleation when the release of CO₂ pressure started (supersaturated CO₂), and cell growth to an equilibrium size during releasing of CO₂;

and, (3) cell stabilization via the cooling process of the foamed system. In the first stage, the pellets form (2.5 mm diameter × 3 mm length) was inserted into an autoclave (96 mL) and the CO₂ pressure was increased up to 10–24 MPa for 5 h at 80 °C. Given such a long time dissolving CO₂ into the sample, CO₂ was completely saturated in the sample at 80 °C.^[3]

In the second stage, upon saturation the samples were removed from the autoclave and brought to atmospheric conditions, and then dipped in a silicone oil bath maintained at the desired foaming temperature T_f , ranging from 80 to 240 °C below and above the glass transition temperature T_g of the virgin matrix polymer for 30 s. After releasing the CO₂ pressure, the formed foams were stabilized via cooling with an ethanol/water mixture (1/1 v/v) to room temperature. The foamed PC/SMA and PCCNs were dried under vacuum at 30 °C to remove the water.

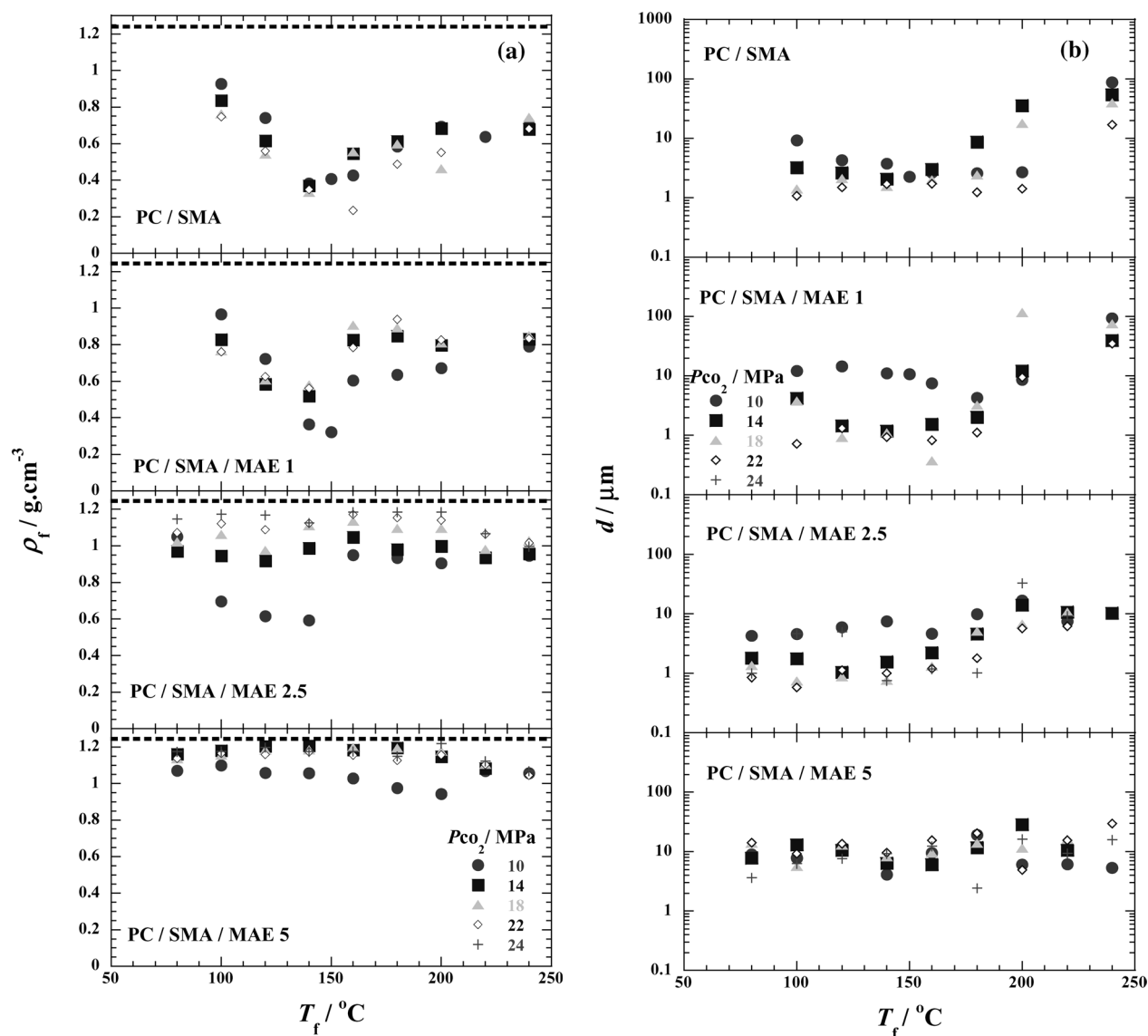


Figure 2. (a) Foaming temperature dependence of foam density (ρ_f) for PC/SMA and PCCNs foams at different pressure conditions. (b) Foaming temperature dependence of cell size (d) for PC/SMA and PCCNs foams at different pressure conditions. (c) Foaming temperature dependence of cell density (N_c) for PC/SMA and PCCNs foams at different pressure conditions.

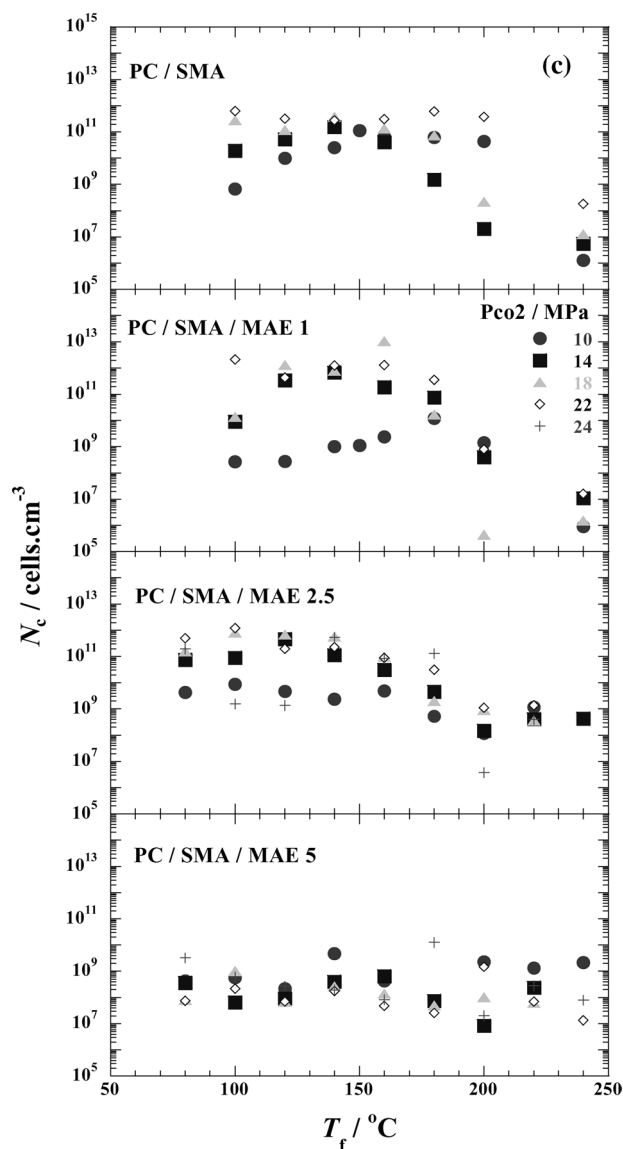


Figure 2. (Continued)

Foam Characterization

The cell structures were investigated by using a scanning electron microscope (SEM) (JSM-5310LV, JEOL), operated at an accelerating voltage of 15 kV. The test samples for SEM were fractured in liquid nitrogen and coated with 20 nm of gold under a pressure of 0.1 Torr for 3 min at a current of 10 mA. The mass density ($\text{g} \cdot \text{cm}^{-3}$) of both pre-foamed ($\rho_p = 1.270 \text{ g} \cdot \text{cm}^{-3}$) and post-foamed (ρ_f) samples were estimated by using the method of buoyancy. The average cell size (d) in mm was determined from the SEM observations. Almost all samples obeyed the Gaussian distribution. The function for determining cell density (N_c) in $\text{cells} \cdot \text{cm}^{-3}$ is given in Equation (1)^[4]

$$N_c = 10^3 \frac{6[1 - (\rho_f/\rho_p)]}{\pi d^3} \quad (1)$$

On the other hand, the mean cell wall thickness (δ) in μm was estimated by Equation (2)^[4]

$$\delta = \frac{d}{2} \frac{1}{\sqrt{1 - (\rho_f/\rho_p)} - 1} \quad (2)$$

Thermomechanical Analysis (TMA)

The compressive modulus of PC/SMA and various PCCNs foams were measured by using TMA (TMA4010S, Bruker AXS K. K.), operated at ambient temperature. The analysis was performed via “the program displacement mode” with a strain rate of $0.01 \text{ mm} \cdot \text{min}^{-1}$ up to strain of 3% of the test sample’s thickness.^[1] The shape of the test sample was cuboid ($2.3 \times 3.2 \times 1.5 \text{ mm}^3$).

Results and Discussion

Morphology of PCCN Foams

Figure 1 shows the typical results of SEM images of the fracture surfaces of the PC/SMA and PCCNs foamed at 140°C under different isobaric saturation condition (10, 18 and 24 MPa). PC/SMA foams exhibit the polygon closed-cell structures having pentagonal and hexagonal faces, which express the most energetically stable state of polygon cells. Such foam structure was obtained probably because these foams belong to the polymeric foams having high gas phase volume (>0.6).^[4] Obviously, under low saturation CO_2 pressure ($\approx 10 \text{ MPa}$), both PC/SMA/MAE1 and PC/SMA/MAE2.5 foams exhibit larger cell size compared with PC/SMA, indicating the dispersed clay particles hinder CO_2 diffusion by creating a maze or a more tortuous path.^[3] However, high CO_2 pressure ($\approx 24 \text{ MPa}$) provides a large supply of CO_2 molecules, which can subsequently form a large population of cell nuclei upon depressurization. The incorporation of nanoclay hinders CO_2 diffusion and simultaneously induces heterogeneous nucleation because of a lower activation energy barrier compared with homogeneous nucleation.^[5]

Here, we calculated the distribution function of cell size from SEM images. Almost all samples obeyed the Gaussian distribution. Cell density and cell wall thickness are calculated by Equation (1) and (2), respectively. Figure 2(a–c) shows the foam density (ρ_f), cell size (d), and cell density (N_c) versus foaming temperature (T_f) under various CO_2 pressures. In case of temperature dependence of ρ_f [Figure 2(a)], PC/SMA, PC/SMA/MAE1, and PC/SMA/MAE2.5 foams indicate a complex tendency. That is, the foam density decreases with increasing T_f up to 140°C , and after that, again increases with T_f under high and low CO_2 pressure. From the above results, such behavior of foam density is due to the competition between the cell nucleation and the cell growth. In the temperature dependence of cell size [Figure 2(b)], we can observe the same temperature dependence in especially PC/SMA and PC/SMA/MAE1. On the other hand, the temperature dependence of cell density [Figure 2(c)] shows the opposite

behavior compared with the tendency of d owing to the cell growth and the coalescence of cells, which usually takes place at high T_f range due to the low viscosity of the systems. This behavior is prominent for PC/SMA/MAE1 due to the action of the heterogeneous nucleation as a dominant factor with increasing CO_2 pressure because of more homogeneous and fine dispersion of clay particles.^[3] For PC/SMA/MAE5, no temperature dependence of N_c is seen, might be indicating the rigidity of the matrix polymer with high MAE loading (5 wt.-%) (see Table 1).

Figure 3 shows d and N_c versus clay content at 140°C under various CO_2 pressure conditions. Under high CO_2 pressure range (14–24 MPa), the value of d decreases with clay content and increases again beyond 1 wt.-% loading. When we compare PC/SMA/MAE1 with PC/SMA, the cell density increases with increasing clay content, suggesting the dispersed clay particles act as nucleating sites for cell formation and lowering of cell size.

From the above results, the excellent cell structure can be obtained with low clay content because of heterogeneous

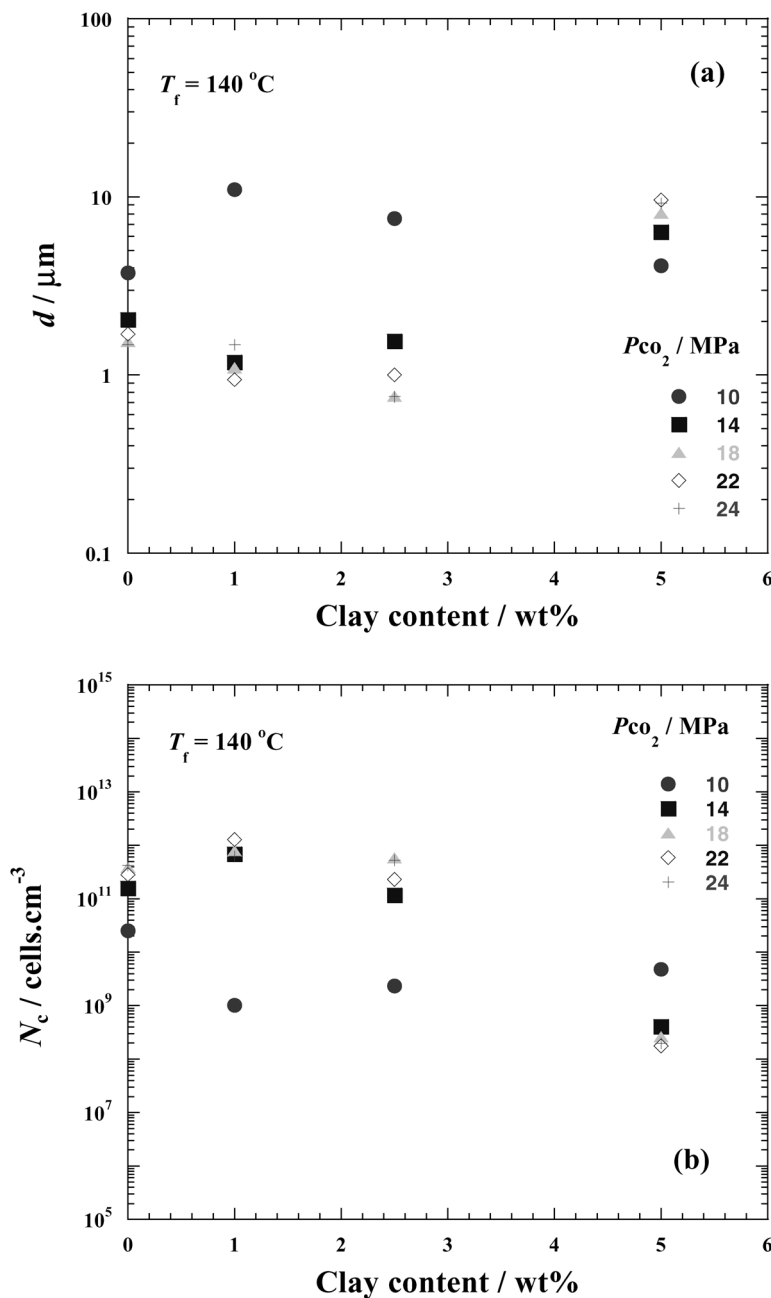


Figure 3. Clay content dependence of (a) cell size (d); and, (b) cell density (N_c) for PC/SMA and PCCNs foamed at 140°C .

nucleation, whereas it cannot be obtained with high clay content because of the matrix rigidity.

Dissolved CO₂ and T_g Depression

Now we turn our discussion to the glass transition temperature T_g depression. To clearly investigate the melt viscosity, we should understand the residue of CO₂ in the samples after depressurization. According to Henry's law,^[6]

$$C_s = H(T)P_{CO_2} \quad (3)$$

where C_s is the gas concentration at saturation, H(T) is the Henry's law constant, and P_{CO₂} is the CO₂ saturation pressure. The temperature dependence of H can be expressed by an Arrhenius-type equation:

$$\ln\left(\frac{H(T)}{H_0}\right) = \frac{E_a}{R} \left(\frac{1}{T} - \frac{1}{T_0}\right) \quad (4)$$

where H₀ and T₀ are the Henry's constant and temperature for STP (= 19.57 × 10⁻³ g CO₂ · g⁻¹ · MPa⁻¹), respectively, and E_a is the activation energy (= 16.13 kJ · mol⁻¹).^[7,8] First we determined H(T) in the temperature range 50–150 °C before determining the gas concentration at various saturation pressures. Figure 4 shows some examples of equilibrium gas concentration versus saturation pressure. Furthermore, according to Chow's model,^[9] we can predict the T_g of the polymer/gas mixture from

$$\ln\left(\frac{T_g}{T_{g0}}\right) = \beta[(1 - \theta) \ln(1 - \theta) + \theta \ln(\theta)] \quad (5)$$

$$\theta = \frac{M_p}{2M_{CO_2}} \frac{w}{1 - w} \quad (6)$$

where T_{g0} is the T_g without gas, M_p and M_{CO₂} are the molecular weights of repeating units in PC and CO₂, respectively, and w is the weight fraction of gas. β is related to the heat capacity by

$$\beta = \frac{2R}{M_p \Delta C_p} \quad (7)$$

where ΔC_p is the specific heat change at T_g (= 0.245 J · g⁻¹ · K⁻¹).^[10] As the above results, the T_g depression of PC is shown in Figure 5. The increase in the diluent (CO₂) concentration reduces T_g monotonously. High CO₂ pressure condition (20 MPa at 80 °C) provides a large supply of CO₂ molecules (14 wt.-%) where the T_g depression occurs up to 75 °C. The significant depression in T_g greatly reduces the melt viscosity and increases the mobility of polymer chains.

Using T_g depressions (corresponding to ΔT_g), we reconstructed plots of ρ_f, d, and N_c versus T_f + ΔT_g from data of Figure 2. The results are shown in Figure 6. This Figure shows that the data nicely conform to a reduced curve compared with Figure 2. The intermediate T_f condi-

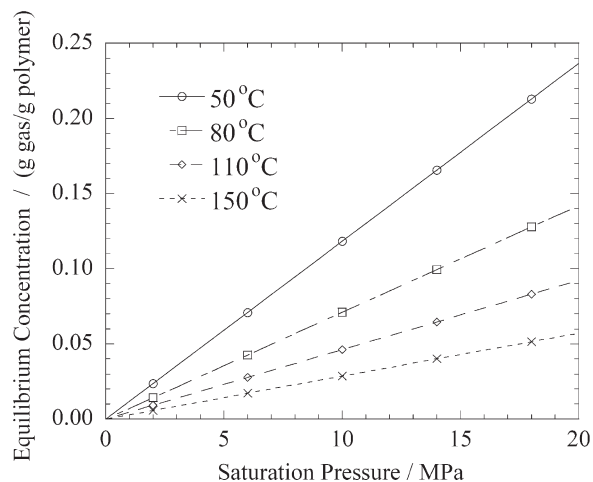


Figure 4. Equilibrium CO₂ gas concentration versus saturation pressure.

tion (≈140 °C) corresponds to a much higher processing temperature (≈200 °C). This indicates that T_g depression is important in optimizing foam processing condition.

In Figure 7, we show the relations between d and N_c, and δ and d. Equation (1) and (2) lead to these relations but some deviation occurs in each system. For example, PC/SMA/MAE2.5 exhibits smaller value of N_c under the same d value when we compare with PC/SMA and PC/SMA/MAE1. For the relation of δ and N_c, PC/SMA/MAE2.5 shows a large value of δ compared with PC/SMA/MAE1. These deviations indicate that the heterogeneous cell distribution mechanism due to the rigid matrix phases in PC/SMA caused by high MAE loading (2.5–5.0 wt.-%), as seen in Figure 1.

Characterization of Interfacial Tension

Both homogeneous and heterogeneous nucleation mechanism may appear to be of comparable significance. All

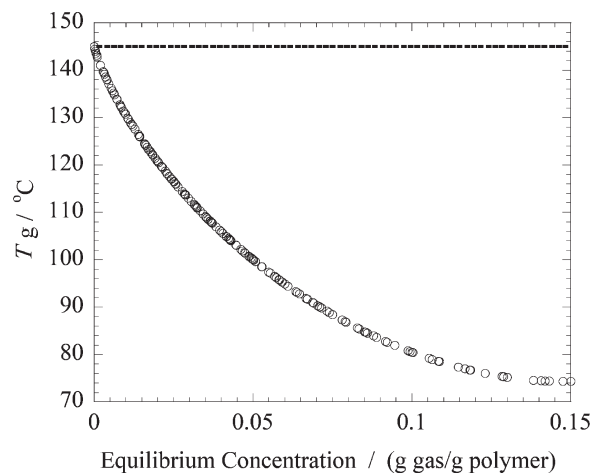


Figure 5. Glass transition temperature depression of PC versus CO₂ concentration.

systems demonstrate that N_c increases systematically with increasing in T_f up to 140 °C. The cell nucleation in the heterogeneous nucleation system such as PC/SMA/MAE foams took place in the boundary between the matrix and the dispersed nanoclay particles. Accordingly, the cell size decreases without individual cell coalescence for PC/SMA/MAE and PC/SMA systems as seen in Figure 6(c).

To clearly investigate the influence of internal surfaces of the dispersed nanoclay that hinders CO₂ diffusion by creating a more tortuous diffusive pathway, we characterized the interfacial tension between bubble and matrix by using modified classical nucleation theory.^[51] According to the theory proposed by Suh and Colton, the rate of nucleation of cells per unit volume (\dot{N}) can be written as

$$\dot{N} \sim C f \exp\left(\frac{-\Delta G}{k_B T}\right) \quad (8)$$

where C is the concentration of CO₂ and/or the concentration of heterogeneous nucleation sites, f is the collision frequency of CO₂, ΔG is the activation energy barrier, k_B is the Boltzmann constant and T denotes absolute temperature. Moreover, the activation energy barrier is given by

$$\Delta G = \frac{16\pi\gamma^3 S(\theta)}{3(\Delta P_{CO_2})^2} \quad (9)$$

where γ is the interfacial tension between bubble and matrix, ΔP_{CO_2} is the magnitude of the pressure quench during depressurization and $S(\theta)$ is the energy reduction

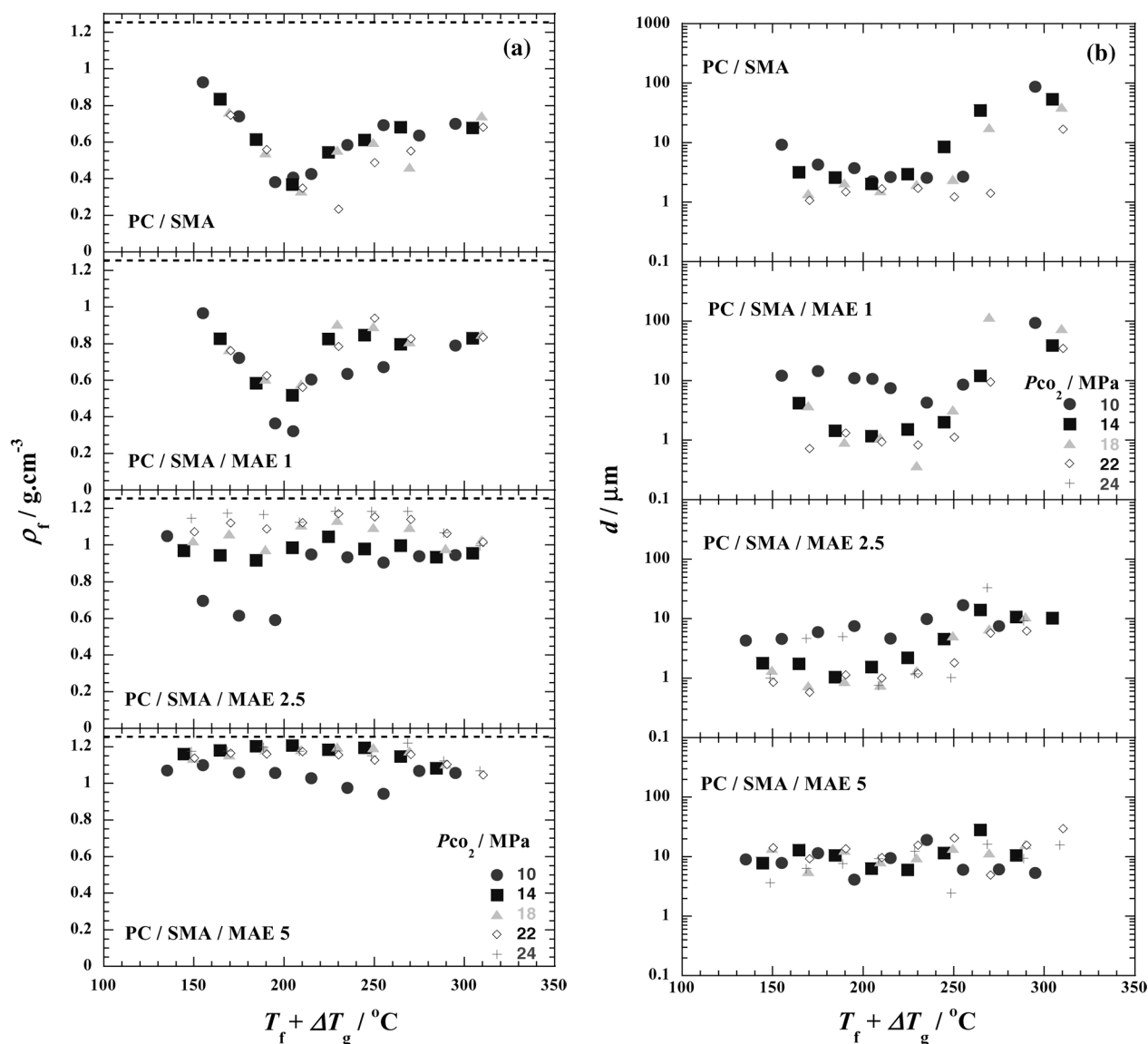


Figure 6. (a) Foam density (ρ_f) versus $T_f + \Delta T_g$ for PC/SMA and PCCNs foams at different pressure conditions. (b) Cell size (d) versus $T_f + \Delta T_g$ for PC/SMA and PCCNs foams at different pressure conditions. (c) Cell density (N_c) versus $T_f + \Delta T_g$ for PC/SMA and PCCNs foams at different pressure conditions.

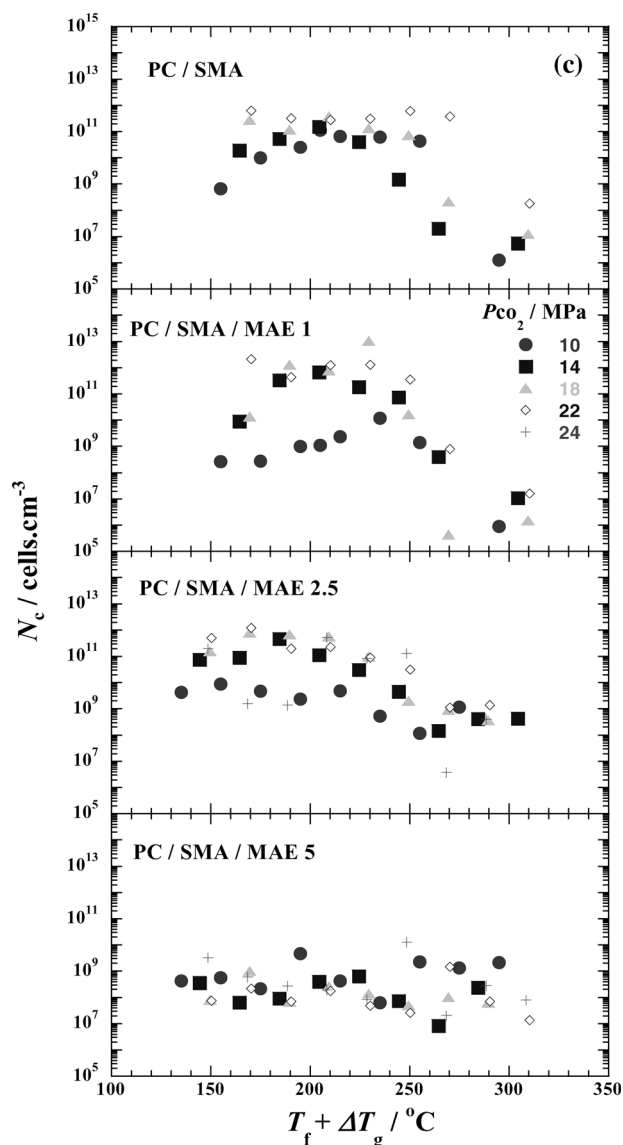


Figure 6. (Continued)

factor for the heterogeneous nucleation (i.e., PC/SMA/MAE). The theoretical cell density is given by

$$N_{\text{theor}} = \int_0^t \dot{N} dt \quad (10)$$

where t is the foaming time that takes 30 s.

At low T_f range (80–140 °C), the value of N_c increase with temperature because the cell growth is prominent. Assuming no effect of the coalescence of cell on the value of N_c , we estimate the interfacial tension of the systems calculated using Equation (8)–(10), that is, the slope of the plots (N_c , versus $1/T_f$).

In Table 2, we summarized the interfacial tension and energy reduction factor of systems calculated using Equation (8)–(10). The interfacial tension of PC/SMA/

MAE1 (including $S(\theta)$ factor) and PC/SMA ($S(\theta) = 1$) are 9.7 and 10.9 $\text{mJ} \cdot \text{m}^{-2}$ at 14 MPa, respectively. These estimated values of γ are in good agreement with that of other poly(methyl methacrylate) (PMMA)-CO₂ system (10–20 $\text{mJ} \cdot \text{m}^{-2}$).^[11] These results are shown in Figure 8(a–b): (a) interfacial tension ($\gamma S(\theta)^{1/3}$) versus clay content under various CO₂ pressure and (b) interfacial tension ($\gamma S(\theta)^{1/3}$) versus CO₂ pressure under different clay content. As shown in Figure 8(a), the interfacial tension slightly decreases with increasing in clay content under same CO₂ pressure condition, indicating heterogeneous cell nucleation occurs easily with increasing in clay content. The estimated reduction factor ($S(\theta) = 0.3$ – 0.8) is same order compared with the foaming of PLA-based nanocomposites.^[12] In Figure 8(b) we observe weak CO₂ pressure dependence of the interfacial tension. The value of $\gamma S(\theta)^{1/3}$ shows a little increment with CO₂ pressure. This result seems to be in conflict with the result in Figure 3(b). However, these are reasonable results when we consider the activation energy barrier, ΔG . As shown in Figure 9, the absolute value of ΔG decreases with CO₂ pressure accompanied with the dependence of the clay content. Therefore, this reasoning is consistent with the explanation for Figure 3(b).

Mechanical Properties of PCCN Foams

Due to the cuboid shape prepared by melt extrusion, the clay particles probably are fixed their face and aligned along the flow (extruded) direction of test specimen. For this reason, we speculated that the orientation of the dispersed clay particles in the sample is well-ordered. We measured compressive moduli in directions both perpendicular and parallel to the flow.

Figure 10 shows the stress-strain curves taken in the direction perpendicular to the flow and strain recovery behavior of the nanocomposites foams and PC/SMA foam prepared with high CO₂ pressure range (18 MPa) at a constant rate of 0.4% min^{-1} . The nanocomposites foam exhibit high modulus compared with PC/SMA foam. The residual strain is around 30–40% as well as PC/SMA foam, providing the excellent strain recovery and the energy dissipation mechanism.^[1]

To clarify whether the modulus enhancement of the nanocomposite foams was reasonable, we applied the following Equation (11) proposed earlier by Kumar^[13] to estimate relative moduli with various foam density:

$$\frac{K_f}{K_p} = \left(\frac{\rho_f}{\rho_p} \right)^4 - \left(\frac{\rho_f}{\rho_p} \right)^2 + \left(\frac{\rho_f}{\rho_p} \right) \quad (11)$$

where K_p and K_f are the modulus of pre-foamed and post-foamed samples, respectively.

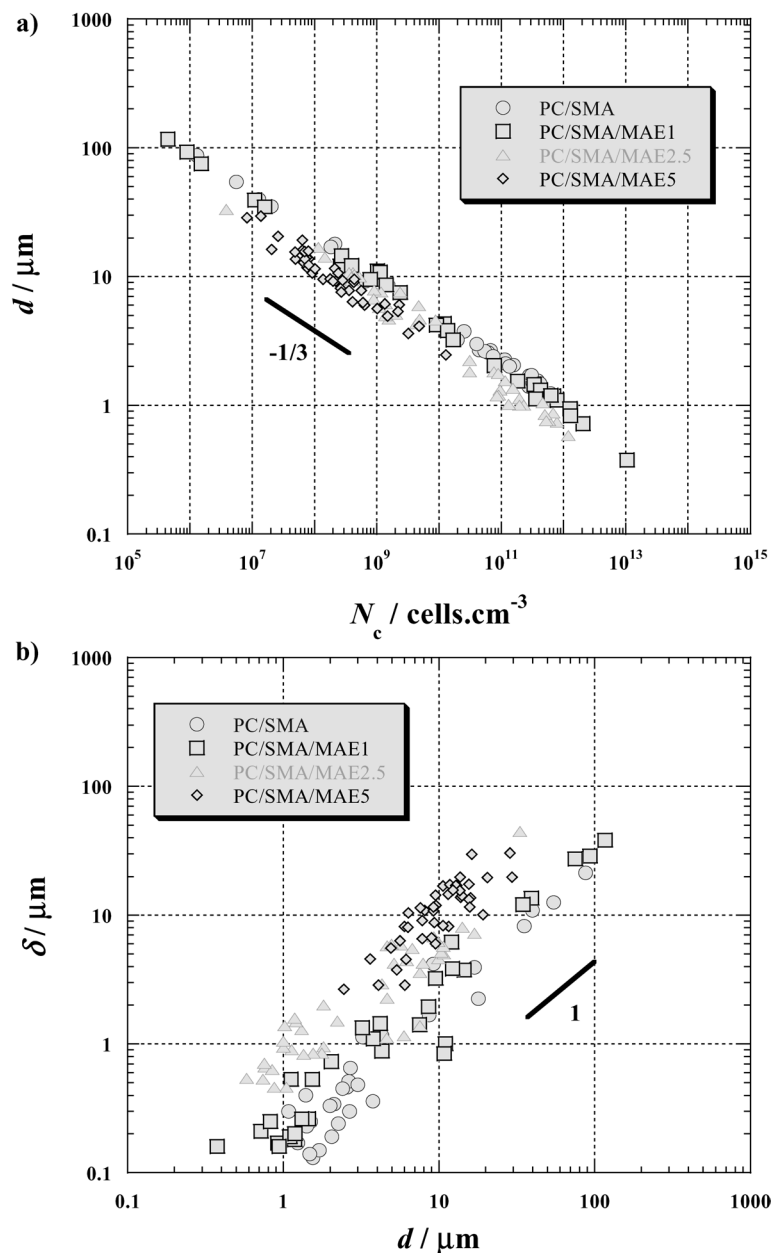


Figure 7. (a) Cell size versus cell density; and, (b) cell wall thickness (δ) versus cell size for PCCNs foams.

Figure 11 shows the relation of relative moduli (K_f/K_p) against relative density (ρ_f/ρ_p) of PC/SMA and PCCNs foams, taken in both directions perpendicular (\perp) and parallel (\parallel) to the flow. This may be because the dispersed clay particles in the cell wall may align along the thickness direction of the sample. In other words, the clay particles arrange due to the biaxial flow of material during foaming.^[1] The solid line in the figure represents the theoretical fit with Equation (11). The relative moduli ($(K_{f\parallel} + K_{f\perp}) / (K_{p\parallel} + K_{p\perp})$) of PC/SMA/MAE1 and PC/SMA foams ex-

hibit higher values than predicted even though they have the same relative mass density. This upward deviation may indicate that the alignment of the dispersed clay particles and the orientation of the polymeric chains taking place during foaming due to the large reduction of the mass density. This creates the improvement in mechanical properties for polymeric foams through polymeric nanocomposites. In case of PC/SMA/MAE1 foams, the clay particles seem to act as a secondary cloth layer to protect the cells from being destroyed by external forces.

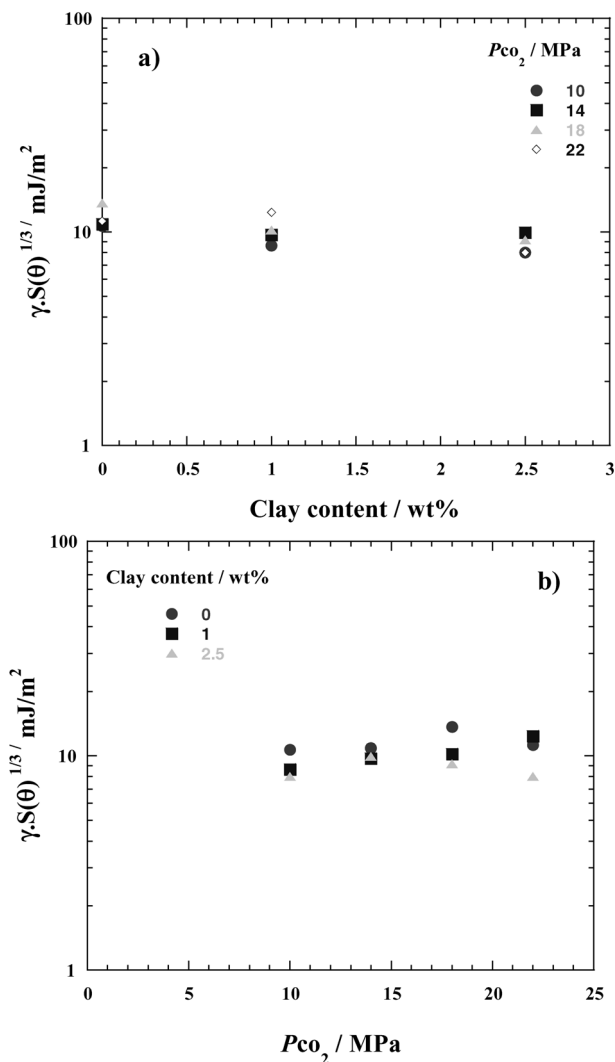


Figure 8. Clay content and CO₂ pressure (P_{CO_2}) dependence of interfacial tension $\gamma S(\theta)^{1/3}$ for PC/SMA and PCCNs foams.

Table 2. Interfacial tension ($\gamma S(\theta)^{1/3}$) including energy reduction factor ($S(\theta)$) of systems calculated using Equation (8)–(10).

Systems	P_{CO_2} / MPa	$\gamma S(\theta)^{1/3}$	$S(\theta)$
		$mJ \cdot m^{-2}$	
PC/SMA-CO ₂	10	10.7	1.0
		8.6	0.53
		8.0	0.42
PC/SMA/MAE1-CO ₂	14	10.9	1.0
		9.7	0.72
		9.9	0.77
PC/SMA/MAE2.5-CO ₂	18	13.6	1.0
		10.2	0.42
		9.2	0.30
PC/SMA-CO ₂	22	11.3	1.0
		12.4	–
		8.0	0.36

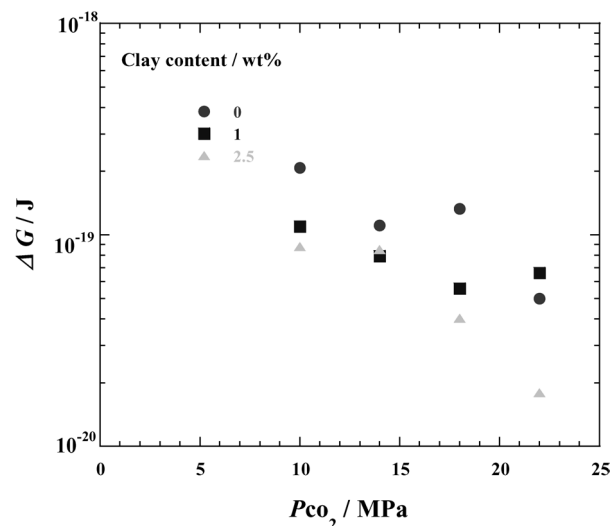


Figure 9. P_{CO_2} dependence of activation energy barrier (ΔG) for PC/SMA and PCCNs foams.

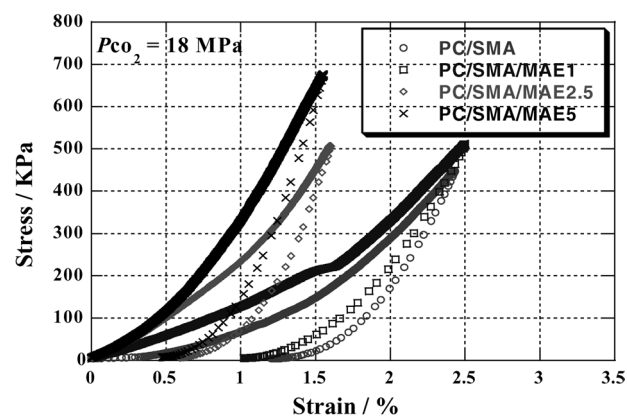


Figure 10. Strain-Stress curve of PC/SMA and PCCNs foamed at 140 °C under 18 MPa.

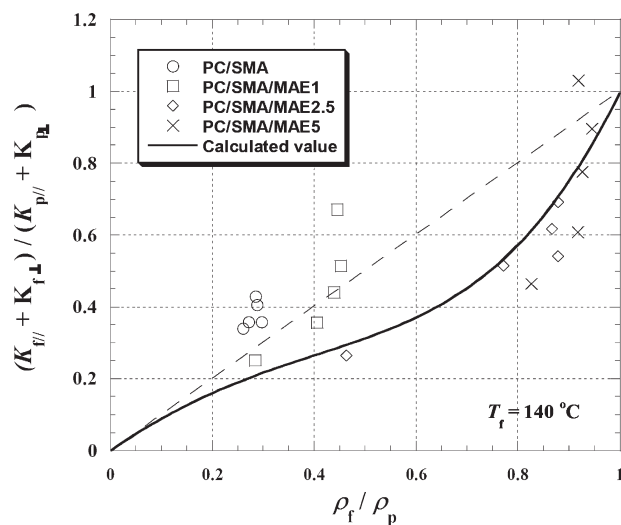


Figure 11. Relative moduli $(K_{f\parallel} + K_{f\perp}) / (K_{p\parallel} + K_{p\perp})$ versus relative density (ρ_f / ρ_p) of PC/SMA and PCCNs foamed at 140 °C. The solid line in the figure represents the theoretical fits based on the Kumar's model.

Conclusion

Under low saturation CO₂ pressure (≈ 10 MPa), both PC/SMA/MAE1 and PC/SMA/MAE2.5 foam exhibited larger cell size compared with PC/SMA, indicating the dispersed clay particles hinder CO₂ diffusion by creating a maze or a more tortuous path. Whereas, under high CO₂ pressure (≈ 24 MPa), both PC/SMA/MAE1 and PC/SMA/MAE2.5 foam exhibited smaller cell size (d), that is, larger cell density (N_c) compared with PC/SMA foam. This reason is a large supply of CO₂ molecules under high CO₂ pressure, which can subsequently form a large population of cell nuclei upon depressurization. In this time, the dispersed clay particles act as nucleating sites for the cell formation and lowering of cell size with clay. In addition, the incorporation of nanoclay-hindered CO₂ diffusion and simultaneously induced heterogeneous nucleation because of a lower activation energy barrier compared with homogeneous nucleation. For PC/SMA/MAE5, no temperature dependence of N_c was seen, might be indicating the rigidity of the matrix polymer with high MAE loading (5 wt.-%). From these results, the excellent cell structure could be obtained with low clay content because of heterogeneous nucleation, whereas it could not be obtained with high clay content because of the matrix rigidity. The controlled structure of the PCCN foams became from microcellular ($d \cong 20 \mu\text{m}$ and $N_c \cong 1.0 \times$

$10^9 \text{ cells} \cdot \text{cm}^{-3}$) to nanocellular ($d \cong 600 \text{ nm}$ and $N_c \cong 3.0 \times 10^{13} \text{ cells} \cdot \text{cm}^{-3}$).

The relative moduli of PC/SMA/MAE1 and PC/SMA foams showed higher values than predicted even though they have the same relative mass density.

- [1] M. Okamoto, P. H. Nam, M. Maiti, T. Kotaka, T. Nakayama, M. Takada, M. Ohshima, A. Usuki, N. Hasegawa, H. Okamoto, *Nano Lett.* **2001**, *1*, 503.
- [2] P. H. Nam, M. Okamoto, P. Maiti, T. Kotaka, T. Nakayama, M. Takada, M. Ohshima, N. Hasegawa, A. Usuki, *Polym. Eng. Sci.* **2002**, *42*, 1907.
- [3] M. Mitsunaga, Y. Ito, S. Sinha Ray, M. Okamoto, K. Hironaka, *Macromol. Mater. Eng.* **2003**, *288*, 543.
- [4] D. Klempner, K. C. Frisch, "Handbook of Polymeric Foams and Foam Technology", Hanser, Munich 1991.
- [5] J. S. Colton, N. P. Suh, *Polym. Eng. Sci.* **1987**, *27*, 485.
- [6] P. L. Durril, R. G. Griskey, *AIChE J.* **1969**, *15*, 106.
- [7] V. Kumar, J. E. Weller, *ANTEC* **1991**, 1401.
- [8] V. Kumar, J. E. Weller, *Cell. Microcell. Mater.* **1994**, *53*, 255.
- [9] T. S. Chow, *Macromolecules* **1980**, *13*, 362.
- [10] V. B. F. Mathot, *Polymer* **1984**, *25*, 579.
- [11] S. K. Goel, E. J. Beckman, *Polym. Eng. Sci.* **1994**, *34*, 1137.
- [12] Y. Ema, M. Ikeya, M. Okamoto, *Polymer*, in press.
- [13] V. Kumar, M. M. van der Wel, *ANTEC* **1991**, 1406.